buildings

MDPI

Article

Influence of Urban Morphological Characteristics on Street-Level Urban Heat Risk: A Geographically Weighted Machine Learning Approach

Yuqiao Zhang [1], Jun Wu [1,*], Kewei Zhong [2], Shengbei Zhou [3], Yankui Yuan [2], Qi Wang [4] and Yuning Liu [1]

[1] School of Architecture, Tianjin Chengjian University, Tianjin 300380, China; 18522566933@163.com (Y.Z.); dorisning_27@163.com (Y.L.)
[2] International School of Engineering, Tianjin Chengjian University, Tianjin 300380, China; zhongkewei2002@163.com (K.Z.); yankui_yuan@163.com (Y.Y.)
[3] School of Architecture, Tianjin University, Tianjin 300072, China; shengbeizhou@163.com
[4] College of Landscape Architecture and Tourism, Hebei Agricultural University, Baoding 071000, China; wikiwang0421@hebau.edu.cn
* Correspondence: wujuntj@tcu.edu.cn

Abstract

As extreme heat events become increasingly frequent worldwide, there is an urgent need for fine-scale assessment of urban heat risk and for identifying its key determinants. Conventional approaches often struggle to capture complex intra-urban spatial heterogeneity, limiting effective heat risk governance and resource allocation. This study applies the Hazard–Exposure–Vulnerability–Adaptation (HEVA) framework by integrating remote sensing, road network, and socio-demographic data. Using the CRITIC weighting method, we quantify and map a street-level heat risk index (HRI) in Tianjin, China. We further employ geographically weighted machine learning models to identify dominant drivers and to characterise nonlinear effects, interaction patterns, and spatially varying relationships. Model reliability is assessed by benchmarking geographically weighted models against global nonlinear baselines under three-fold cross-validation; GW-XGBoost achieves comparable explanatory power to the best global model (R^2 = 0.672) while yielding lower prediction errors (MAE = 0.142), supporting robust spatial inference. Results show that elevated heat risk is not confined to the urban core; instead, it is more pronounced in peripheral transitional zones around central districts. These areas often exhibit coincident heat stress and high population exposure, a higher concentration of vulnerable groups and ageing residential neighbourhoods, and comparatively limited access to medical and cooling resources. Mechanistically, greater development intensity is generally associated with higher heat risk, whereas higher vegetation cover tends to reduce risk; however, the strength and, in some locations, the direction of these effects vary substantially across streets. These findings suggest that heat risk management should prioritise peripheral transitional zones. Targeted interventions should balance development intensity, expand effective greening and shading, and improve the provision and accessibility of healthcare and cooling services to reduce street-level heat risk.

Keywords: heat risks; geographically weighted machine learning model; driving factors; spatial heterogeneity; urban thermal environment

Check for updates

Academic Editor: Jiying Liu

Received: 26 January 2026
Revised: 8 February 2026
Accepted: 9 February 2026
Published: 11 February 2026

Copyright: © 2026 by the authors. Licensee MDPI, Basel, Switzerland. This article is an open access article distributed under the terms and conditions of the Creative Commons Attribution (CC BY) license.

1. Introduction

Anthropogenic warming is substantially increasing the frequency, duration, and intensity of extreme heat events. In urban areas, heat exposure is often compounded by high population density and the urban heat island effect, making urban heat risk one of the most immediate and pressing public health challenges under climate change [1,2]. A large multi-country epidemiological study estimated that non-optimal ambient temperatures account for approximately 7.71% of all deaths globally, and that heat-related impacts tend to be amplified in more urbanised settings [3]. Attribution analyses across 43 countries further suggest that around 37% of summer heat-related deaths can be attributed to anthropogenic climate change, translating into tens to hundreds of additional heat-related fatalities annually in many regions [4]. Evidence from Chinese cities echoes this vulnerability: projections indicate that annual urban heat-related deaths could reach 1.037–1.299 million under 1.5 °C of global warming, increasing to 1.373–1.699 million under 2.0 °C warming [5]. Against this backdrop, the World Health Organization has promoted Heat–Health Action Plans as a cornerstone of urban health governance and climate adaptation, emphasizing systematic risk assessment, early warning systems, and targeted protection of vulnerable populations [6]. Collectively, these findings underscore the urgency of integrating heat-risk reduction into urban development and planning.

Urban heat risk is shaped not only by regional climate warming but also by local urban morphological and land cover configuration. Using data from 85 Indian cities, Mondal and Anand [7] reported a clear positive association between heat exposure risk and urban morphological characteristics; within high-density megacities, reduced green space and expanded impervious cover emerged as key contributors to elevated heat exposure. Such attributes modify the surface energy balance by altering heat absorption, storage, and release, thereby producing pronounced intra-urban variability in heat conditions within the same city [8,9]. Consistent evidence from the United States further highlights this heterogeneity and its social patterning: an analysis of 175 major urbanised areas found systematic disparities in heat exposure within nearly all cities, with disadvantaged populations more likely to reside in higher-risk zones [10].

A central challenge in urban heat risk management is to determine which intra-urban spatial units bear the greatest heat burden during heatwaves and to identify the factors that jointly shape this risk. To address this need, researchers have increasingly operationalised heat risk through indicator-based frameworks that decompose risk into measurable components and enable empirical assessment at the city scale [11]. However, key drivers of heat risk are often simultaneously nonlinear and spatially heterogeneous. As a result, achieving fine-grained risk identification while retaining model interpretability remains a major methodological challenge in urban heat risk assessment.

As a foundational framework in heat risk research, the Crichton risk triangle [12] continues to be widely used to conceptualise heat risk as the combined effect of three core elements: heat hazard, heat exposure, and heat vulnerability [13,14]. Building on this triadic structure, more recent and refined assessment frameworks have been proposed to better capture the full risk formation process. For example, the HEVA framework extends the risk triangle by incorporating heat adaptability (often conceptualised as adaptive capacity) as a fourth component, alongside heat hazard, exposure, and vulnerability [15].

With expanding data availability, heat risk assessments are achieving progressively higher spatiotemporal resolution and becoming better aligned with the operational needs of urban governance. For example, Delina and Chen [16] applied a risk matrix approach to evaluate heat hazard risk at the national scale across 77 Romanian cities. In China, Wu [17] integrated multi-source remote sensing and socioeconomic datasets to map heat risk across the Yangtze River Delta. Despite these advances, most existing studies still

rely on relatively coarse spatial units (e.g., municipalities or districts), which can mask substantial intra-urban variability and thereby constrain the development of fine-grained, targeted risk management strategies and intervention designs [18].

In constructing and weighting composite heat risk indices, including heat hazard, heat exposure, heat vulnerability, and heat adaptability, equal weighting (EW) and principal component analysis (PCA) remain the two most widely used approaches [19–21]. EW is appealing for its simplicity and reproducibility, but it cannot readily reflect differences in indicator importance or potential interdependencies among indicators. PCA can partially address multicollinearity by transforming correlated variables into orthogonal components; however, the physical and social meaning of these components is often difficult to interpret consistently across study contexts, which may undermine cross-regional comparability. Consequently, the transparency of weighting decisions and the robustness of composite indices remain recurrent points of debate in comprehensive heat-risk assessments.

Meanwhile, urban morphological characteristics are increasingly recognised as a pivotal entry point for advancing heat risk research. Heat risk is ultimately grounded in heat-related hazards, and the spatial pattern of the urban heat environment provides a direct physical manifestation of where such hazards emerge and persist. Accumulating evidence indicates that urban morphological features not only influence heat conditions but also shape the spatial organisation of heat environments within cities. For example, multi-city analyses have reported systematic associations between urban morphological characteristics and the intensity of surface urban heat islands [22]. Using a global dataset of 1113 built-up areas, Chen [23] further showed that built environment density (BD) and building height (BH) nonlinearly modulate the cooling efficiency of urban green space. Despite this growing body of evidence on heat environments, the systematic integration of urban morphological characteristics into heat risk assessments remains relatively underexplored, and comparable quantitative evidence across contexts is still limited. Importantly, evidence on heat environments does not directly translate into evidence on composite heat risk, because heat risk is jointly shaped by heat hazard, exposure, vulnerability, and adaptive capacity, as well as their interactions.

When examining the relationship between urban morphological characteristics and heat risk, the choice of regression approach is an important methodological consideration. Early studies commonly relied on traditional regression techniques, including linear regression [24,25]. However, these models often have limited flexibility in representing nonlinear associations, marginal effects, and interaction patterns among variables. Accordingly, machine learning methods have attracted growing attention in recent years because they can characterise complex nonlinear relationships in large datasets [26]. At the same time, researchers have increasingly noted that many machine learning models are specified as global models, which can make it difficult to reflect spatial heterogeneity in heat risk and the possibility of locally varying relationships [27]. In response, geographically weighted machine learning approaches have become more widely used [28,29]. For instance, the geographically weighted XGBoost model (GW-XGBoost) fits a separate local XGBoost regression at each spatial location and commonly uses feature importance metrics to support model interpretation [30]. By allowing model relationships to vary across space, GW-XGBoost is well suited for settings where geographic non-stationarity may be present, and it has been applied in areas such as health and transport studies [31].

Nevertheless, differences in methodological choices and spatial modelling strategies can substantially affect how relationships between urban morphological characteristics and heat risk are identified and interpreted, and they therefore offer a clear entry point for refining subsequent research questions. Frist, the construction of composite heat risk indices and their core components, including heat hazard, heat exposure, heat vulnerability,

and heat adaptability, still largely relies on weighting schemes such as EW or PCA. These approaches often have limited capacity to reflect interdependencies and interaction patterns among indicators. Accordingly, there is a need to further explore alternative weighting strategies to strengthen the scientific rigour and reliability of heat risk assessments [32]. Second, although many studies have improved data resolution, analytical units are frequently defined at relatively coarse scales, such as cities or districts, which can constrain support for fine-grained and targeted risk management and intervention design. Third, while a substantial body of quantitative evidence links urban morphological characteristics to variations in the heat environment, empirical research remains limited on how these characteristics are associated with heat risk itself and whether these associations vary in magnitude or direction across locations.

To address these gaps, the theoretical novelty of this study does not lie in adding methodological complexity per se, but in proposing a coupled research pathway that combines heat risk construction with mechanism-oriented inference. Specifically, we operationalise street-level heat risk under the HEVA framework using multi-source indicators and a modified CRITIC weighting strategy that integrates variability, correlation structure, and entropy-based information content, and implement geographically weighted machine learning (GW-XGBoost) to reveal nonlinear, spatially varying, and interaction effects of urban morphology on heat risk. This combination enables new substantive insights by distinguishing where high hazard is offset (or not) by adaptive resources and by identifying which morphological factors matter most—and in what direction—across different neighbourhood contexts.

Specifically, the study addresses the following questions: (1) What is the spatial pattern of street-level heat risk in Tianjin under the HEVA framework? (2) Which urban morphological characteristics are most strongly associated with higher or lower heat risk? (3) To what extent can geographically weighted machine learning methods characterise marginal effects, interaction patterns, and spatial heterogeneity in the associations between urban morphological characteristics and heat risk?

Taking Tianjin as a case study, this research identifies street-level heat risk hotspots and highlights urban morphological characteristics that are most strongly associated with spatial variations in heat risk. The findings provide spatially explicit evidence to inform heat risk prevention and resilient urban development, and they offer a transferable reference for other cities seeking fine-scale heat risk assessment and policy design.

2. Study Area and Data

2.1. Study Area

Tianjin Municipality is located in the eastern North China Plain and is one of China's four directly administered municipalities, with distinctive geographic conditions and an urban structure shaped by rapid development. According to official statistics for 2023, Tianjin covers approximately 11,966 square kilometres [33] and administers 16 districts [34]. In 2023, the permanent resident population was about 13.82 million. With a high population density and intensive urban development, Tianjin represents a typical high-density municipality undergoing rapid urbanisation [35]. Tianjin has a temperate monsoon climate, featuring hot and humid summers and cold winters. In recent years, summer heatwave conditions in the city may have been reinforced by ongoing urbanisation and broader climatic warming, together with relatively limited vegetation and water bodies in some built-up areas. This study uses 306 street-level units across Tianjin as the analytical units, covering subdistricts and several functional zones.

As shown in Figure 1c, the land cover map indicates a pronounced imbalance in land-use composition within Tianjin's central urban districts. Impervious surfaces dominate

much of the central area, whereas vegetation cover, including tree cover and grassland, is more concentrated toward peripheral zones. Vegetation within the central urban area is relatively fragmented, which may reduce local climate regulation capacity and is often associated with stronger urban heat island effects and heightened heat stress during extreme heat events. Consequently, the central urban area is likely to face elevated heat risk in summer, particularly given its dense population and intensive economic activities, alongside comparatively constrained ecological buffering capacity.

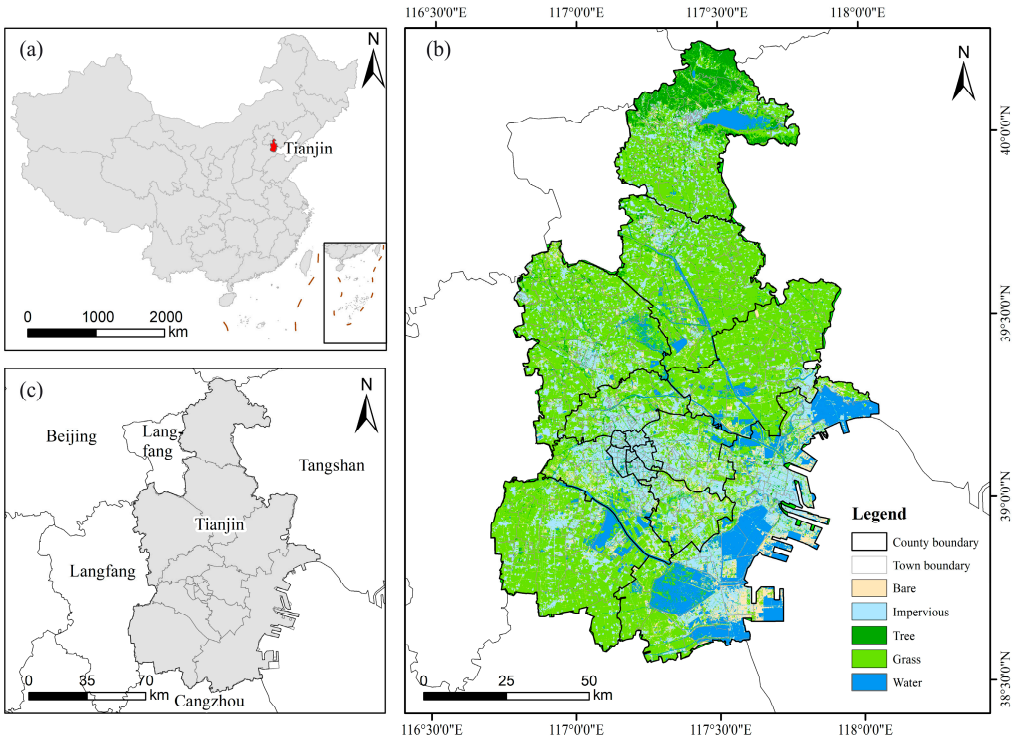

Figure 1. Study area location: Tianjin, China. (**a**) Tianjin is located in the north of China. (**b**) Tianjin overview. (**c**) Land-use classification in Tianjin.

2.2. Data Sources

This study uses streets as the primary analytical unit. The dataset is organised into two categories: (1) variables used to construct the component indicators of the HRI and (2) independent variables representing urban morphological characteristics. Most datasets correspond to the year 2020, which was selected because both remote sensing products and socioeconomic data are relatively complete and internally consistent for that period. Although the China Multi-Attribute Building (CMAB) dataset was released in 2022 and the housing value data were compiled from an online platform in 2023, the relevant variables used in this study were processed to represent conditions in 2020; meanwhile, the spatial resolution of raster-based datasets was standardised to 30 m. Heat environment variables are mainly derived from satellite remote sensing products. Land surface temperature was retrieved from Landsat 8 using the Google Earth Engine platform. Surface parameters were obtained from the Chinese Academy of Sciences (CAS) 2020 NDVI dataset. Land cover and landscape pattern indicators were extracted from ESA WorldCover 2020. Population exposure variables were derived from WorldPop 2020 raster data and were further combined with age group information to represent the spatial distribution of susceptible populations. Urban built environment variables include road network density, calculated from OpenStreetMap road data. Building morphology was derived from the 3D-GloBFP dataset [36], and building age was obtained from the CMAB dataset [37]. For the socioeconomic and service facility dimension, POI data were used to characterise the intensity of facility provi-

sion and functional clustering. POIs were further filtered to identify healthcare services and heat relief facilities as proxies for response resources. Economic development levels were obtained from CAS GDP-related data products [38], and internet-sourced housing price data were used to supplement spatial differences in residents' economic capacity. Collectively, these datasets provide the empirical basis for constructing heat risk indicators and characterising urban morphological characteristics.

Regarding preprocessing, all spatial datasets were first harmonised to a consistent coordinate reference system and clipped to the study area boundary. Raster and vector layers were then aggregated to street level. Subsequently, point-based datasets, including POIs and housing prices, were cleaned and classified through deduplication and correction of abnormal coordinates. POIs were further filtered by function to identify healthcare services and heat relief facilities, and the resulting indicators were normalised to generate comparable street-level metrics. Finally, the small number of missing values was handled using a consistent procedure, yielding a complete street-level dataset for heat risk estimation and subsequent model development.

To examine the relationship between heat risk and its potential determinants, this study uses the heat risk index (HRI) as the dependent variable. This requires a scientifically robust and conceptually coherent assessment framework. A widely adopted approach is the Cutter Risk Triangle, which conceptualises heat risk in terms of three core components: heat hazard, heat exposure, and heat vulnerability [39–41]. Specifically, (1) heat hazard refers to the potential threat posed by natural or anthropogenic events that can adversely affect public health, property, and the environment; (2) heat exposure describes the presence and distribution of people, ecosystems, environmental resources, infrastructure, or other assets in locations that may be affected by heat-related impacts; and (3) heat vulnerability denotes the degree to which a system or population is susceptible to harm or has limited capacity to cope, often reflected in the concentration of vulnerable groups.

To establish a more comprehensive assessment framework, scholars have proposed the "Hazard–Exposure–Vulnerability–Adaptability" (HEVA) heat risk assessment system [15]. This framework incorporates (4) adaptability, encompassing mitigation measures (such as the layout of medical and cooling facilities) and adaptation (linked to economic development levels) to enhance the integrity of heat risk mapping. It is generally recognised that heat hazard, heat exposure, and heat vulnerability collectively elevate regional heat risk, while heat adaptation helps mitigate the adverse effects of the former three [41–43]. Accordingly, the HRI can be expressed as the summation and offsetting relationship of four primary indicators:

$$HRI = HHI + HEI + HVI - HAI \quad (1)$$

In Equation (1), HRI denotes the heat risk index, with higher values indicating greater risk; HHI represents the heat hazard index; HEI signifies the heat exposure index; HVI indicates the heat vulnerability index; and HAI reflects the heat adaptability index.

This study initially identified 13 secondary indicators for constructing the HRI. Specifically, the hazard dimension includes land surface temperature (LST). The exposure dimension includes population density, POI density, road network density, and the spatial distribution of microblog check-ins. The vulnerability dimension includes child population density, elderly population density, female population density, and building age. The adaptability dimension includes GDP, the density of heat relief facilities, the density of medical facilities, and housing prices.

During data preparation, we used correlation analysis to screen candidate indicators [44]. Among the initial set of HRI indicators, strong correlations were observed between POI density and the spatial distribution of Weibo check-ins, as well as between elderly population density and female population density. To reduce redundancy while

retaining informative variables, we compared these paired indicators in terms of data coverage and relevance. POI data provide larger volumes and broader spatial coverage, whereas Weibo check-ins are more concentrated in commercial areas and may not represent all demographic groups consistently. We therefore retained POI density and excluded the Weibo check-in indicator. Similarly, given evidence that older adults and young children tend to be more sensitive to extreme weather than females as a demographic category [45], we retained elderly population density and removed female population density. Ultimately, 11 secondary indicators were selected to construct the HRI (Table 1).

Table 1. Indicators considered in the heat risk assessment framework and their data sources.

First-Level Indicators	Abbreviation	Second-Level Indicators	Data Sources
Heat hazard index	HHI	Land surface temperature (LST) (°C)	2020 Landsat 8
Heat exposure index	HEI	Population density	2020 Worldpop
		POI density	2020 AutoNavi Open Platform
		Road network density	2020 OpenStreetMap (OSM)
Heat vulnerability index	HVI	Child population density	2020 Worldpop
		Elderly population density	2020 Worldpop
		Year of construction	2022 A Multi-Attribute Building Dataset of China (CMAB)
Heat adaptability index	HAI	Housing value	2023 Website
		Heat avoidance facilities density	POI density
		Medical facilities density	POI density
		GDP	2020 Chinese Academy of Sciences (CAS)

We selected nine urban morphological characteristics as independent variables (Table 2). These variables capture multiple facets of urban form and were quantified across four aspects: building morphology, landscape composition, surface parameters, and landscape pattern.

During the initial indicator screening, we derived three building form metrics, namely, average building height (BH), building density (BD), and floor area ratio (FAR). We also defined four landscape composition indicators: impervious surface ratio (ISR), vegetation ratio (VR), water area ratio (WR), and soil ratio (SR). In addition, four widely used landscape pattern indicators were selected, including edge density (ED), largest patch index (LPI), mean patch area (AREA), and perimeter/area ratio (PARA). As surface parameters, we included the Normalised Difference Vegetation Index (NDVI) and the Normalised Difference Building Index (NDBI). As shown in Figure A1, Pearson correlation analysis indicated strong correlations among BH, BD, FAR, ISR, and NDBI, suggesting potential multicollinearity. To reduce redundancy and improve model stability and interpretability, we further compared these variables and selected a single representative measure. FAR was retained as the indicator of building morphology because it can reflect, to some extent, both horizontal development intensity and vertical development level, thereby summarising information captured by building height and building density. Accordingly, BH, BD, ISR, and NDBI were not included in subsequent analyses.

Notably, the HEVA indicators used to construct the HRI (Table 1) do not include any urban morphological variables; morphological characteristics are introduced only as external predictors in the GW-XGBoost models (Table 2). Therefore, the two variable sets do not overlap, and circularity is avoided by design.

Table 2. Urban morphological characteristics and data sources.

Categories of Variables	Variables (Abbreviation)	Formula	Description	Data Sources
Building morphology	Floor area ratio (FAR)	$FAR = \frac{\sum_{i=1}^{n}(c \times F)}{A}$	Floor area ratio of buildings within the analysis unit, representing the overall building development intensity	2020 3D-GloBFP
Landscape composition	Vegetation ratio (VR)	$VR = \frac{A_{veg}}{A}$	Percentage of vegetated area (e.g., trees, shrubs, grass) within the analysis unit	2020 ESA WorldCover
	Waterbody ratio (WR)	$WR = \frac{A_{water}}{A}$	Percentage of waterbody area (e.g., rivers, lakes, ponds) within the analysis unit	2020 ESA WorldCover
	Soil ratio (SR)	$SR = \frac{A_{soil}}{A}$	Percentage of bare soil or sparsely vegetated area within the analysis unit	2020 ESA WorldCover
Landscape pattern indices	Edge density (ED)	$ED = \frac{\sum_{j=1}^{N} p_j}{A}$	Total perimeter of green land patches per hectare within the analysis unit	2020 ESA WorldCover
	Largest patch index (LPI)	$LPI = \frac{a_{max}}{A}$	Proportion of the largest green land patch within the analysis unit	2020 ESA WorldCover
	Mean patch area (AREA)	$AREA = \frac{1}{N}\sum_{j=1}^{N} a_j$	Average area of green land patches within the analysis unit	2020 ESA WorldCover
	Perimeter/area ratio (PARA)	$PARA = \frac{1}{N}\sum_{j=1}^{N}\left(\frac{p_j}{a_j}\right)$	Average perimeter/area ratio of green land patches within the analysis unit	2020 ESA WorldCover
Biophysical parameters	Normalised Difference Vegetation Index (NDVI)	$NDVI = \frac{\rho_{NIR}-\rho_{Red}}{\rho_{NIR}+\rho_{Red}}$	Mean value of the Normalised Difference Vegetation Index within the analysis unit, indicating the level of vegetation greenness and biomass	2020 Chinese Academy of Sciences (CAS)

Note: A—area within each analytical unit; c—number of floors; F—floor area of the building; p_j—perimeter of the jth vegetation patch in a block unit; a_{max}—area of the largest patch (i.e., the patch with the maximum area) among all patches within the analysis unit; a_j—area of the jth patch; ρ_{NIR}—reflectance in the near-infrared band; ρ_{Red}—reflectance in the red band.

3. Methods

3.1. Research Framework

This study uses Tianjin Municipality as a case study to develop an integrated framework for heat risk assessment and for analysing its associated driving mechanisms. The overall workflow is summarised in Figure 2. First, drawing on prior studies, we adopted the HEVA heat risk assessment system to guide the initial selection of indicator categories. Candidate indicators were then screened using correlation analysis, resulting in 11 secondary indicators as the basis for subsequent calculations. We applied a modified CRITIC method to derive indicator weights, computed four primary components, and aggregated them to generate a street-level heat risk map. Next, we used XGBoost to examine the associations between urban morphological characteristics and the HRI, and we visualised modelled relationships using partial dependence plots (PDPs). Finally, we compared several geographically weighted models and selected the geographically weighted XGBoost model (GW-XGBoost). Model interpretation was further supported by SHAP to characterise marginal effects, interaction patterns, and spatial heterogeneity in the associations between urban morphological characteristics and heat risk, based on feature importance, interaction diagnostics, and local contributions.

3.2. Weighting of HRI

Given the diverse data sources and indicator types, substantial differences in scale and magnitude make standardisation necessary to ensure comparability and the validity of subsequent calculations. All variables were aggregated to street-level units. Positive indicators, including heat hazard, heat exposure, and heat vulnerability, and negative indicators, represented by heat adaptability, were normalised using min–max scaling

(range normalisation). The normalisation formulas for positive and negative indicators are given in Equations (2) and (3), respectively.

$$X_{nor} = \frac{X_t - X_{\min}}{X_{\max} - X_{\min}} \tag{2}$$

$$X_{nor} = \frac{X_{\max} - X_i}{X_{\max} - X_{\min}} \tag{3}$$

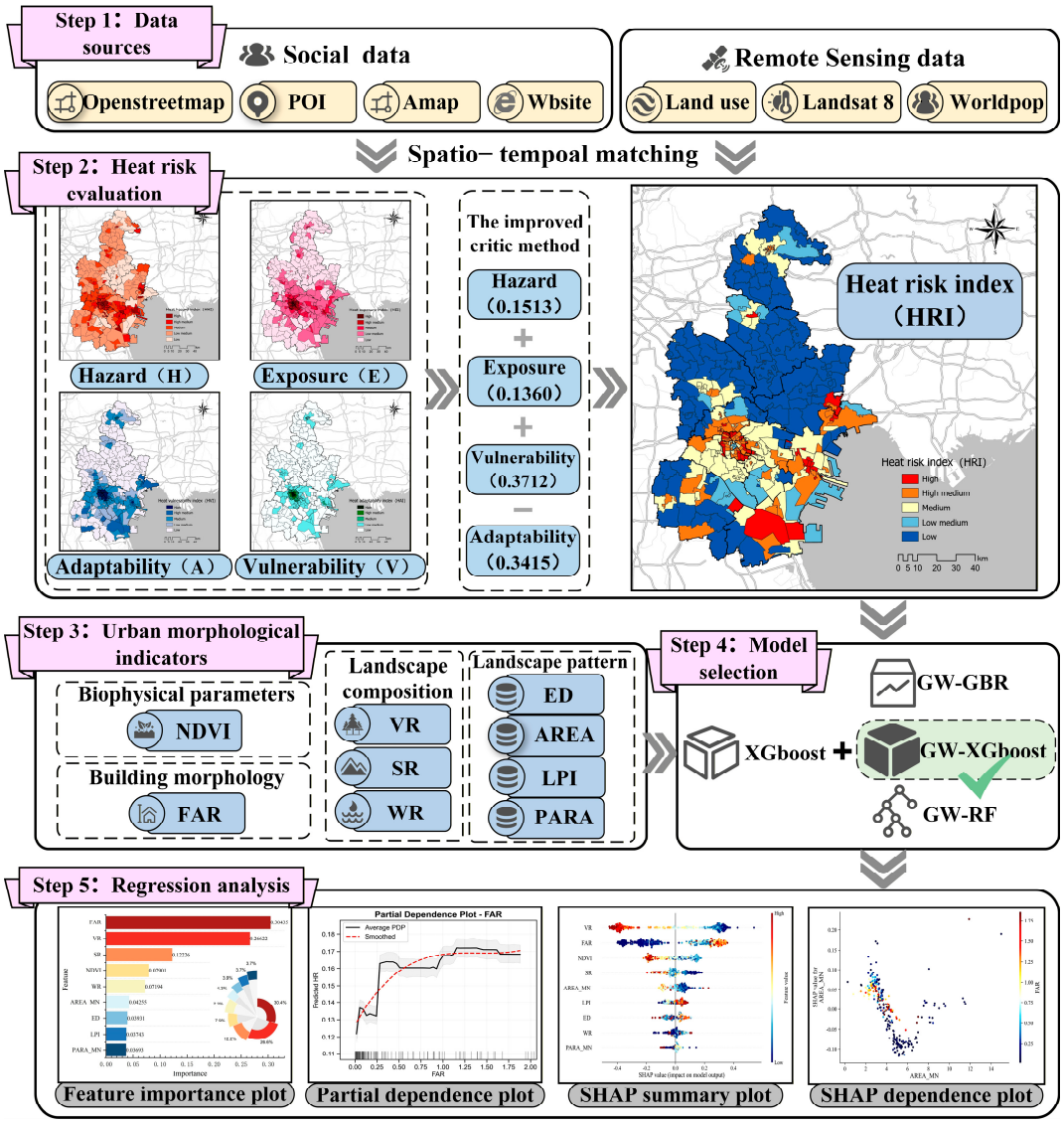

Figure 2. Research framework.

In the equations, X_{nor} denotes the standardised value of the indicator, X_i represents the raw value of indicator i, $X_{\min}$ indicates the minimum value of indicator i, and $X_{\max}$ denotes the maximum value of indicator i.

When assessing the relative importance of HRI-related indicators, many studies rely on the Analytic Hierarchy Process (AHP), which involves expert judgement and can introduce subjectivity [46], or they apply equal weights across primary indicators [13,14,47]. However, the four primary HRI components may contribute differently to overall heat risk, and the underlying indicators can be correlated with one another. These features highlight the need for a quantitative and data-driven weighting scheme. Accordingly, this study

adopts a modified CRITIC method (Table 3), which considers both indicator variability and inter-indicator correlations. By incorporating an entropy-based measure of information content, the method captures the degree of dispersion in each indicator while accounting for redundancy due to correlation. In contrast to purely judgement-based approaches, the modified CRITIC method derives weights from the objective statistical properties of the data, thereby providing a more transparent basis for indicator weighting.

Table 3. Combined weights of heat risk indicators.

First-Level Indicators	Weight of First-Level Indicators	Second-Level Indicators	Weight of Second-Level Indicators
Heat hazard index	0.1513	Land surface temperature (LST) (°C)	1
Heat exposure index	0.1360	Population density	0.2213
		Point of Interest density	0.2481
		Road network density	0.5306
Heat vulnerability index	0.3712	Child population density	0.3084
		Elderly population density	0.1
		Year of construction	0.5916
Heat adaptability index	0.3415	Housing value	0.1503
		Heat avoidance facilities density	0.2301
		Medical facilities density	0.3394
		GDP	0.2802

3.3. Model Construction and Interpretation

To investigate potential nonlinear relationships between urban morphological characteristics and heat risk, we developed and compared six nonlinear models, including three global models (XGBoost, RF, and GBR) and three geographically weighted models (GW-XGBoost, GW-RF, and GW-GBR). Model performance was evaluated using R^2, RMSE, MAE, and MedAE, with higher R^2 and lower error values indicating better performance.

Based on the comparative results, we first selected the best-performing global model, XGBoost, and used partial dependence plots (PDPs) to examine how individual features were associated with variation in HRI. Given the potential spatial heterogeneity in the relationships between heat risk and its determinants, we further selected the best-performing geographically weighted model, GW-XGBoost, and used SHAP for additional interpretation.

Among the three global models, XGBoost achieved the strongest performance, with an R^2 of 0.692 and the lowest RMSE, indicating slightly better overall explanatory capacity and fit than RF (R^2 = 0.677) and GBR (R^2 = 0.631). After introducing geographic weighting, GW-XGBoost produced an R^2 of 0.672, which was only marginally lower than that of XGBoost, while yielding the lowest MAE and MedAE across all models. This pattern suggests that GW-XGBoost reduced mean and median prediction errors and may better accommodate local variability and outlying observations, while still supporting model interpretation.

A combined review of R^2 and error metrics suggests that XGBoost provides the strongest overall fit, whereas GW-XGBoost performs better in controlling prediction errors and improving stability. The two models show broadly comparable performance, but GW-XGBoost can offer additional value by characterising spatial heterogeneity in modelled relationships. Given this study's emphasis on street-level variation in heat risk drivers, and the reliance of subsequent analyses on local feature importance and spatially explicit visualisation, GW-XGBoost provides a practical balance between predictive performance and spatial interpretability. It is therefore selected as the primary model for subsequent analyses and scenario assessment.

XGBoost is an ensemble learning algorithm under the gradient boosting framework and is widely used for regression and classification, particularly in settings with high

dimensional features. By integrating Classification and Regression Trees (CART) into a boosting structure, XGBoost can flexibly model nonlinear associations and interaction patterns that are difficult to represent with linear models. It therefore often achieves strong predictive performance and can be less sensitive to correlated predictors than many conventional regression specifications [48,49]. During training, the model iteratively fits residuals across boosting rounds by minimising an objective function. Regularisation terms are included, and additional constraints on tree complexity are applied to reduce overfitting and support generalisation. The XGBoost formulation is given in Equation (4):

$$\hat{y}_i = \sum_{k=1}^{K} f_k(x_i),\ f_k \in \mathcal{F} \tag{4}$$

In Equation (4), the prediction function is represented in the form of an additive tree ensemble as $\hat{y}_i = \sum_{k=1}^{K} f_k(x_i)$. Here, i denotes the sample index, x_i is the feature vector of the i-th spatial unit, and $\hat{y}_i$ is the model's predicted value for the target variable of this sample. k represents the total number of regression trees in the ensemble; f_k denotes the function corresponding to the k-th CART regression tree, where $f_k \in \mathcal{F}$ indicates that each tree originates from the predefined tree function space $\mathcal{F}$. Thus, the model is collectively formed by a set of structurally constrained regression trees.

The GW-XGBoost model extends the conventional XGBoost framework by incorporating spatial heterogeneity into the modelling process. Drawing on the core idea of geographically weighted regression, it supports local analysis of how associations may vary across space. Specifically, GW-XGBoost fits a separate local XGBoost model at each observation location using a subset of neighbouring samples, with their contributions determined by a spatial weighting scheme. This local calibration strategy is intended to better accommodate spatial non-stationarity and to facilitate interpretation of spatially varying relationships. The GW-XGBoost formulation is given in Equation (5):

$$\hat{y}_i = F_{s_i}(x_i) = \sum_{k=1}^{K} f_{k,s_i}(x_i) \tag{5}$$

In Equation (5), $\hat{y}_i$ denotes the predicted value for the i-th spatial unit, x_i represents the feature vector for that unit, and s_i indicates the geographical coordinates of that unit; $F_{s_i}(\cdot)$ is the local prediction function trained at location s_i, emphasising that model parameters and structure may vary with spatial position, thereby capturing spatial non-stationarity. In the equation, k denotes the number of regression trees within each local model, while $f_{k,s_i}(\cdot)$ represents the k-th CART regression tree at location s_i, whose output constitutes an incremental contribution to the prediction value. The final prediction result for that location is formed by accumulating the outputs from each tree. Unlike global XGBoost, the key feature of GW-XGBoost lies in explicitly incorporating spatial indices (f_{k,s_i}) and spatial weighting (s_i). This enables each location's model to undergo local calibration using neighbouring samples under distance-weighted constraints. Consequently, the ensemble structure and variable-response relationships may differ across locations, revealing spatial heterogeneity in how urban morphological characteristics influence HRI.

To mitigate overfitting and ensure model generalisability, we combined out-of-sample evaluation with cross-validated complexity control for both the global XGBoost and GW-XGBoost models. The dataset was split into a training and a held-out test set (70/30; random_state = 42), and model performance was reported on the test set. Key XGBoost hyperparameters included the number of trees (n_estimators), maximum tree depth (max_depth), learning rate (learning_rate), subsample ratio (subsample), and feature subsampling ratio (colsample_bytree). These parameters, which directly regulate model complexity and

variance, were tuned using Optuna with three-fold cross-validation on the training set. The objective was to minimise the mean RMSE across folds, and 150 trials were conducted. The resulting optimal configuration was then used to train the global XGBoost model. All other parameters were kept at their default settings, and the random seed was set to 42.

For GW-XGBoost, a local submodel was fitted for each street unit using samples from its nearest neighbours, with observations weighted by an adaptive bi-square kernel based on Haversine distance. The bandwidth of the local window was defined by the number of nearest neighbours. A three-fold cross-validation search over candidate bandwidths was performed, and the optimal bandwidth was selected by minimising the average RMSE. To avoid overly local fits, this bandwidth selection ensures sufficient local sample support. The optimal hyperparameters obtained for the global XGBoost model were then applied to each local submodel, thereby controlling complexity consistently across space while allowing for spatially varying associations between urban morphological characteristics and heat risk to be characterised.

4. Results

4.1. Spatial Distribution of HRI

Figure 3a–d present the spatial distributions of the four primary indicators, namely, heat hazard, heat exposure, heat vulnerability, and heat adaptability. Using the natural breaks (Jenks) classification, each indicator was grouped into five levels: low, lower, medium, higher, and high. To quantitatively examine whether the spatial pattern of the HRI reflects a genuine spatial structure, we assessed spatial autocorrelation using Global Moran's I (Appendix B). The results indicate a significant positive spatial autocorrelation in HRI (Moran's I = 0.211, p = 0.001), suggesting that street-level heat risk is spatially clustered rather than randomly distributed.

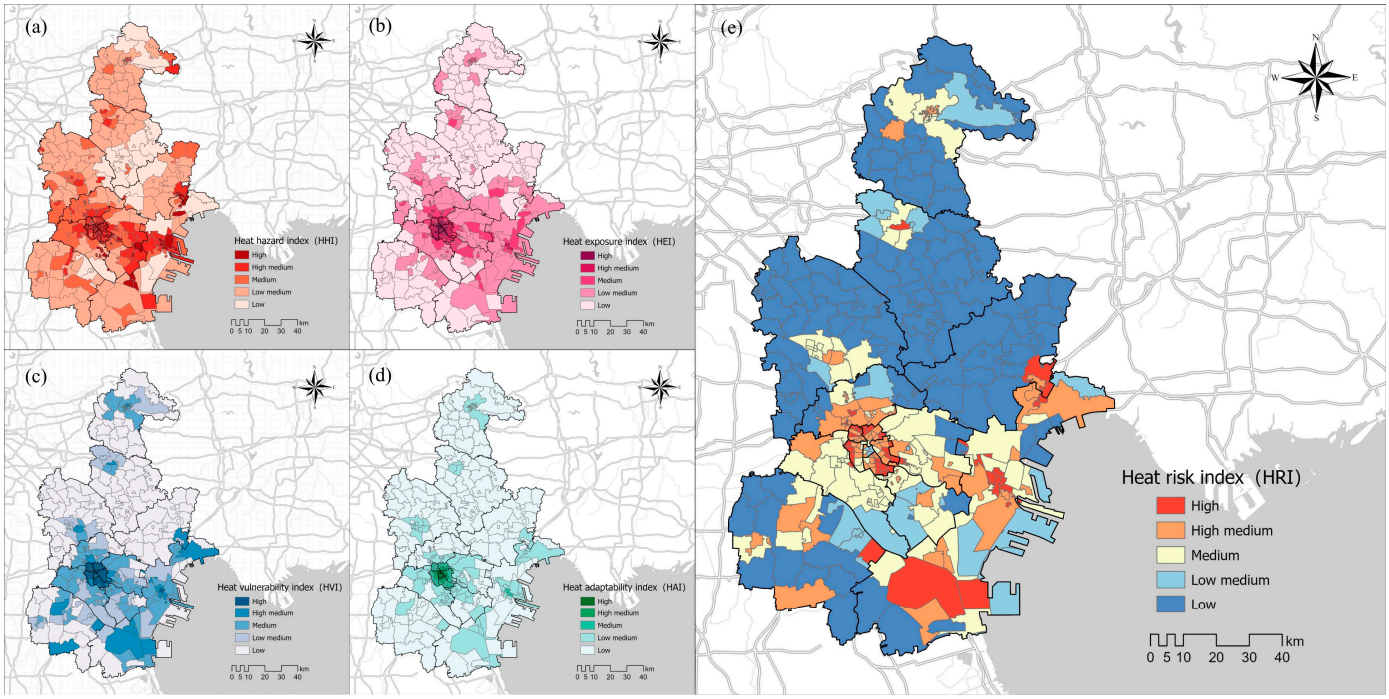

Figure 3. (**a**) Spatial distribution of HHI; (**b**) spatial distribution of HEI; (**c**) spatial distribution of HVI; (**d**) spatial distribution of HAI; (**e**) spatial distribution of HRI.

HHI shows contiguous areas of high and moderately high values in the central urban districts and in parts of the southeastern Binhai New Area, whereas streets in the north

and in peripheral areas are dominated by low and moderately low values. This pattern is consistent with the relatively higher impervious surface ratios in central and coastal zones, where dense built-up forms and heat-absorbing materials are more prevalent. By contrast, northern and peripheral streets, which include larger proportions of vegetated and forested land, tend to exhibit lower HHI values.

A broadly similar pattern is observed for HEI, with high values concentrated in central urban streets. This distribution may be associated with dense residential populations, high-intensity clusters of POIs that indicate substantial commercial and service activity, and relatively dense road networks. These central streets also accommodate substantial commuting and consumption activity, which corresponds to a larger population potentially exposed to heat stress during hot periods. In contrast, most northern streets and peripheral southwestern areas show low or moderately low HEI levels, with only scattered medium or higher values in some county-level towns and subdistrict centres. These locations are more likely to be characterised by agricultural or ecological land, lower population density, fewer POIs, and sparser road networks, which aligns with generally lower levels of heat exposure.

High and moderately high HVI values are observed across several clusters, including central urban streets, the southern Binhai New Area, northern streets, and parts of Jinghai District. Within the central urban area, high HVI is widespread and is associated with higher concentrations of older adults and children, together with a substantial stock of ageing residential neighbourhoods. Buildings constructed earlier often have comparatively limited thermal performance, which may correspond to higher potential health risks during heatwaves. Notably, Zhaishang Subdistrict in northern Binhai New Area and Haibin Subdistrict in the south show extensive water bodies in the land cover map, yet their HVI remains relatively high. This pattern may reflect the influence of surrounding older residential areas and nearby industrial zones.

High HAI values are concentrated in the central urban districts. These areas contain dense clusters of tertiary hospitals and community healthcare centres, and they are also characterised by higher property prices and GDP levels. In addition, public indoor spaces that can provide cooling and shade, such as commercial complexes and cultural venues, are more abundant than in other subdistricts. Collectively, these features suggest stronger capacity for resource mobilisation and service provision during heat events. By contrast, outlying districts are dominated by low or moderately low HAI levels. These areas are more closely associated with agricultural activities or lower-intensity industries, relatively limited economic output, fewer high-grade medical facilities, and less extensive heat-relief infrastructure, together with lower property values and public service investment. These conditions are consistent with comparatively weaker heat adaptability.

Figure 3e shows the spatial distribution of the HRI in Tianjin. Overall, high and moderately high HRI values are concentrated in the central urban districts and in the northern, central, and southern parts of the Binhai New Area. These locations tend to exhibit relatively high surface temperatures and activity related exposure, together with higher proportions of older adults and children and a larger stock of older buildings. This combination corresponds to elevated heat risk. In the coastal port belt and southern development zones of the Binhai New Area, large industrial parks coexist with residential communities, and both permanent and transient populations are relatively concentrated. However, high-grade medical facilities and public cooling infrastructure are more unevenly distributed and are concentrated in a limited number of service nodes, which aligns with continuous or patchy high-risk clusters.

Within the central urban area, elevated heat risk does not appear to be confined to the most central thoroughfares. Instead, it forms a near circular belt around their periphery.

While the most central streets show the highest levels of heat hazard and exposure, they also concentrate dense and high-grade medical resources and cooling facilities, and their heat adaptability scores are markedly higher than those of surrounding areas. This pattern is consistent with a partial offset of the combined impacts associated with intense heat, high exposure, and population vulnerability. By contrast, peripheral streets around the central thoroughfares show similar levels of heat hazard, exposure, and vulnerability, but they tend to have more limited access to comparable medical services and public cooling spaces. Their heat adaptability is therefore relatively lower, which is associated with higher HRI values. These results suggest that, in highly urbanised settings, strengthening heat adaptability in the urban core alone may be insufficient to reduce heat risk across the broader city. Transitional zones between central and suburban areas merit particular attention in heat risk management and adaptation planning.

Areas with low or moderately low heat risk are mainly located in Tianjin's northern mountainous region and in western and northeastern outlying districts. These areas are dominated by forest, grassland, and agricultural land, which corresponds to lower surface temperatures and lower heat hazard. They also tend to have lower population density, POI density, and road network density, which is consistent with lower exposure. In addition, some subdistricts have a younger age structure and a higher share of newly constructed housing, suggesting lower social vulnerability. Although these areas generally have fewer medical and heat relief facilities and more modest economic conditions, which is consistent with lower heat adaptability, the combined effect of moderate to low levels of hazard, exposure, and vulnerability is associated with overall HRI remaining in the low range.

4.2. Relative Importance Ranking

This study used permutation-based variable importance to examine how individual variables are associated with heat risk [50]. The method randomly permutes the values of each explanatory variable and quantifies the resulting increase in prediction error, measured here by RMSE. Variables that produce larger RMSE increases are considered more important. Figure 4 summarises the relative feature importance for street-level HRI in both models.

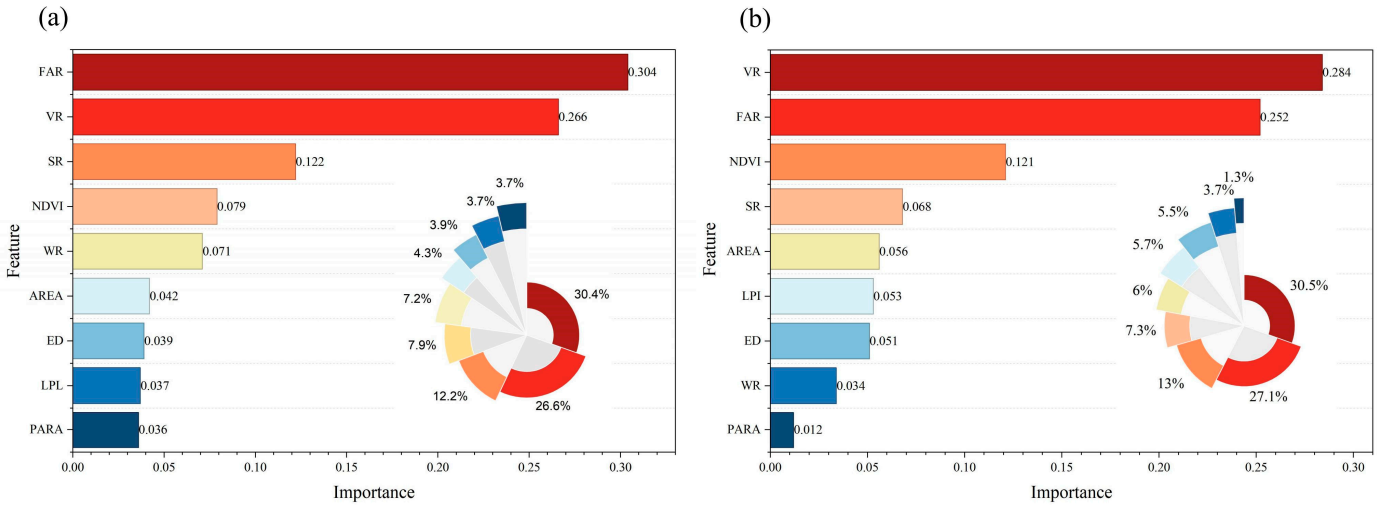

Figure 4. (**a**) Feature importance output from XGBoost; (**b**) Feature importance output from GW-XGBoost.

To examine whether permutation importance rankings are sensitive to sampling variability, we repeated model fitting under the cross-validation setting and computed feature importance within each fold. The results show that the importance rankings of key morphological predictors are consistent across folds: core variables consistently appear among the top-ranked predictors in most repetitions, and overall rank fluctuations

are limited. This indicates that the observed ranking differences between XGBoost and GW-XGBoost are not primarily driven by local sample instability or metric sensitivity, supporting the robustness of our interpretation.

In the global XGBoost model, feature importance is concentrated in a small number of variables. FAR shows the highest importance (0.304), followed by VR (0.266), with SR ranking third (0.122). The remaining variables display a sharp decline in importance. NDVI and WR fall into an intermediate tier, whereas landscape pattern indicators generally rank lower. Overall, this result suggests that, within the global model, variation in street-level heat risk is more strongly captured by indicators describing development intensity and vegetation conditions, while landscape pattern metrics contribute comparatively less to prediction performance.

By contrast, the feature importance ranking changed after geographic weighting was introduced. In the GW-XGBoost model, VR moved to first place (0.284), followed by FAR (0.252), and NDVI (0.121) replaced SR as the third-ranked variable. At the same time, the importance of AREA, LPI, and ED increased in the geographically weighted model, which suggests that these landscape pattern metrics make clearer contributions when relationships are evaluated locally. In contrast, PARA declined further in importance, indicating that patch shape complexity provides a weaker and less consistent contribution to predictive performance in this setting.

These differences are consistent with the modelling logic of the two approaches. Global XGBoost estimates a single set of relationships for the entire study area and therefore emphasises variables that explain overall variation. GW-XGBoost allows for relationships to vary across space through locally fitted models, which can increase the importance of variables that display stronger spatial variability and better discriminate among local contexts. This interpretation is consistent with the higher ranking of VR and NDVI in the geographically weighted model and with the increased importance of several landscape pattern indicators. Overall, both models point to a similar ordering of key variables. FAR and VR remain the most important predictors of street-level heat risk, whereas landscape pattern indicators generally have lower importance in both models, suggesting they are less central to explaining spatial variation in heat risk.

The GW-XGBoost model provides a spatially explicit view of how feature importance varies across locations, enabling assessment of whether the predictive contribution of specific urban morphological characteristics differs among streets. By mapping the spatial distribution of feature importance, dominant factors can be visually identified across the study area. In the maps (Figure 5), blue indicates lower importance and red indicates higher importance.

For FAR, feature importance is relatively high in Shuangkou Subdistrict of Beichen District and in several subdistricts in the western and southern parts of the urban core, while it is lower in northern areas dominated by ecological and agricultural land. This pattern suggests that, in high-density built-up areas, model performance is more sensitive to variation in FAR, whereas in lower density zones with more natural land cover, FAR contributes less to prediction.

Among landscape composition variables, VR shows higher feature importance in Dabaizhuang Subdistrict, Baodi District, and surrounding areas, while the northern mountainous region and many southern subdistricts display lower values. This distribution is consistent with VR playing a more prominent predictive role in some medium density built-up contexts. WR exhibits relatively high feature importance in Chuanyangyu Subdistrict of Jizhou District, around the Yuqiao Reservoir, and in the southeastern Linhai Subdistrict, whereas most other areas show low values. This suggests that water-related variation contributes meaningfully to HRI prediction mainly in specific locations. The spatial pattern

of SR feature importance is more fragmented, with scattered high value patches around Huanghuadian Subdistrict and Nancai Village Subdistrict in Wuqing District, while most other areas remain at medium to low levels.

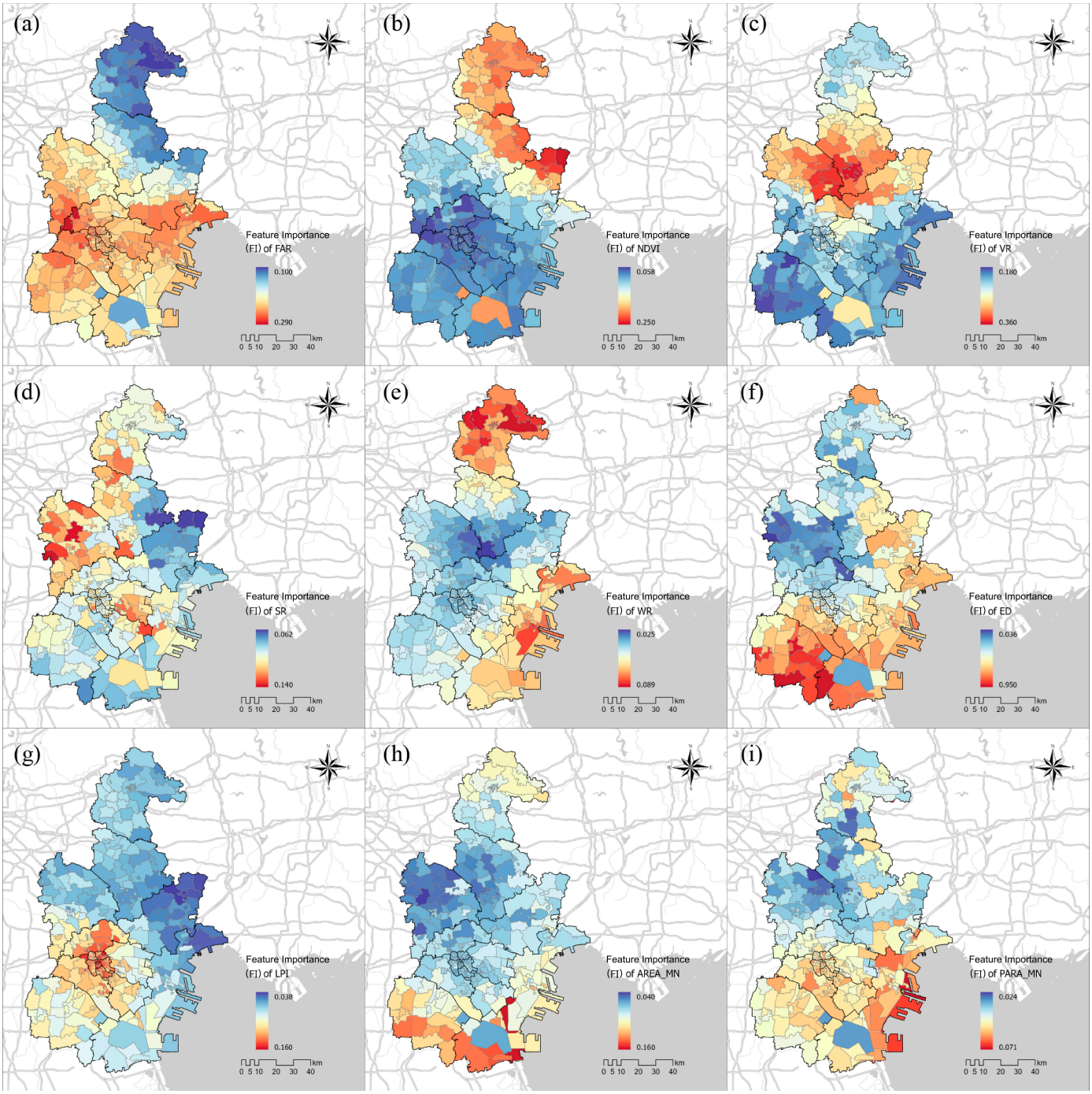

Figure 5. (**a**–**i**): Spatial distribution of local FI for urban morphological characteristics.

Among landscape pattern variables, higher feature importance for AREA and ED is mainly observed in large development zones in the south and southeast. Elevated AREA values are clustered around Gulin Subdistrict and the Light Textile Industrial Zone, while higher ED values are concentrated near Tangguan Tun Subdistrict and Xiaowangzhuang Subdistrict. Northern and western subdistricts generally show low values. This pattern suggests that, within these development zones, model predictions are more sensitive to variation in mean patch area and edge density. Higher LPI feature importance is primarily

observed around central urban subdistricts, whereas northern and northeastern areas show consistently low values. Feature importance for PARA is relatively higher in southeastern coastal and southern subdistricts and lower in northern subdistricts.

As a surface parameter, NDVI exhibits a spatial pattern that contrasts with that of building form related variables. Streets in the northern mountainous region tend to have higher NDVI importance, whereas central urban areas and contiguous built-up areas in the south tend to have lower values. This distribution is consistent with NDVI contributing more to model prediction in ecologically resource rich contexts, while built environment related variables play a larger role in highly urbanised areas.

These spatial contrasts indicate that the relative contributions of different characteristics to heat risk prediction can vary substantially across space, which may help explain why findings differ across studies conducted in different urban contexts. Geographically weighted models provide a useful means of characterising such local variability. In addition, the mean feature importance offers a complementary aggregate perspective by summarising the average contribution of each variable across the entire study area. Higher mean importance suggests that a feature contributes to prediction in a wider range of locations.

4.3. Marginal Effects

Partial dependence plots (PDPs) summarise the average association between a given feature and the model output, conditional on the other variables in the model. In Figure 6, the horizontal axis shows urban morphological characteristics, and the vertical axis shows the standardised HRI. The black curve represents the estimated PDP, the red dashed line shows a fitted smooth curve, and the light grey band indicates the 95% confidence interval. In addition, because observations can be sparse in the tails of several predictors, interpretation of nonlinear turning points and thresholds is restricted to data-dense ranges (5th–95th).

The PDP for FAR indicates that predicted HRI increases rapidly from low FAR values and remains relatively high across the medium to high range. This pattern is consistent with higher development intensity being associated with more enclosed urban spaces and less favourable heat dissipation conditions, which corresponds to higher heat risk in the model. In contrast, the PDP for VR shows a clear threshold like response. Predicted HRI remains elevated when VR is low but decreases sharply and then stabilises once VR exceeds a certain level. This suggests that increases in vegetation coverage are associated with lower heat risk once a minimum level of vegetation is present. Compared with FAR and VR, SR shows an approximately monotonic decline, indicating that higher SR values are associated with lower predicted HRI when other variables are held constant. This pattern may reflect differences in land cover composition and built-up intensity across streets with varying SR levels.

Surface parameter variables mainly show more moderate responses. NDVI exhibits an overall downward trend, suggesting that higher greenness is generally associated with lower heat risk across different urban morphological contexts. However, the confidence band widens notably at medium to high NDVI levels, indicating greater uncertainty and potential heterogeneity in the estimated relationship, which may be related to interactions with other physical and socioeconomic conditions. The remaining variables show smaller PDP amplitudes and wider uncertainty, implying relatively modest contributions to variation in predicted HRI.

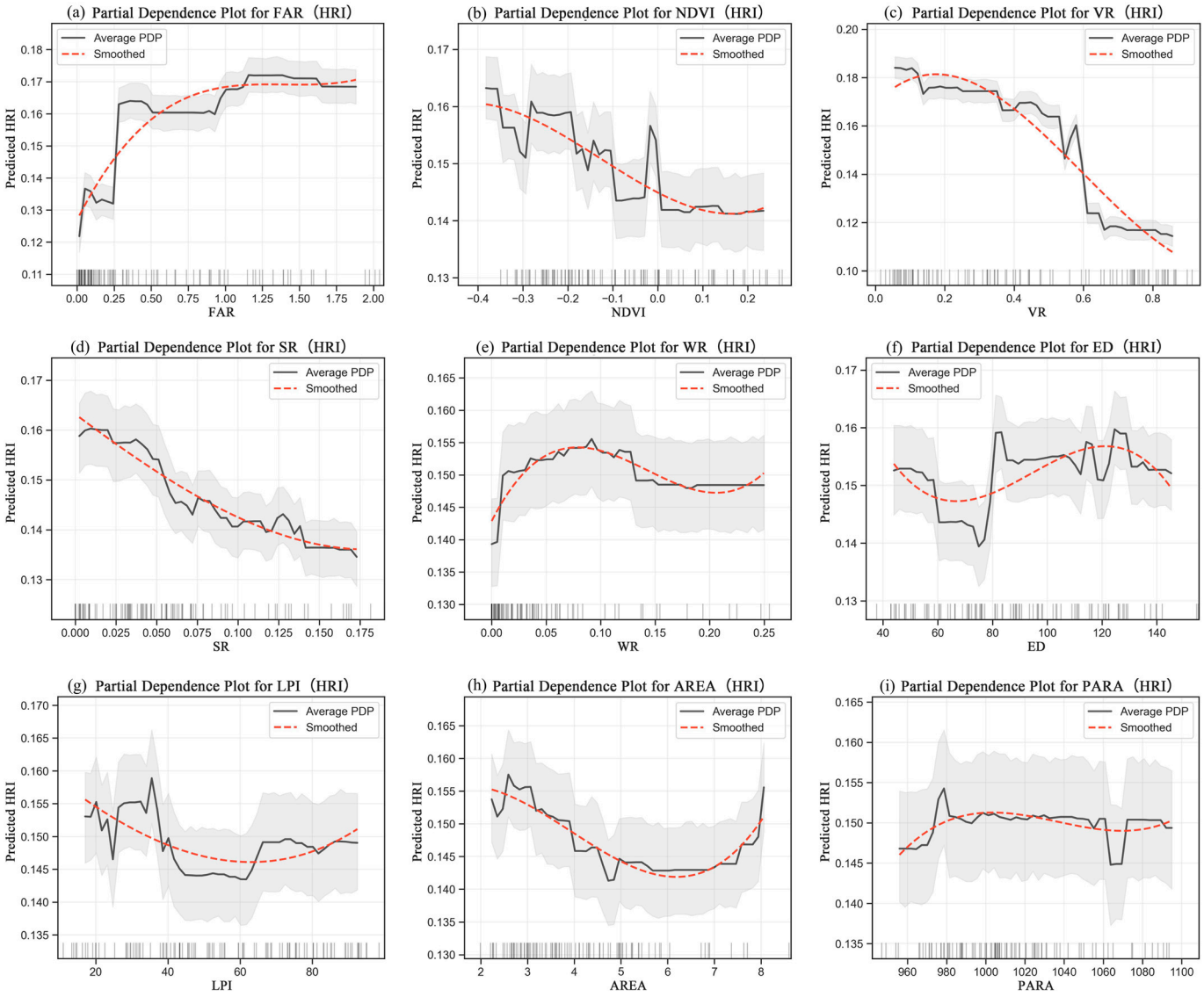

Figure 6. (**a**–**i**) Probability of Downpour (PDP) between urban morphological characteristics and HRI.

4.4. Interaction Effects

To further characterise the directional contributions of urban morphological characteristics to heat risk prediction and to examine potential interaction patterns, this study applies SHAP interpretation to the GW-XGBoost model. The SHAP summary swarm plot (Figure 7) visualises the distribution of contributions for each variable across samples. The horizontal axis shows SHAP values, which represent the contribution of a feature relative to the model's baseline prediction for a given sample. Positive SHAP values indicate that the feature is associated with a higher predicted HRI for that sample, whereas negative values indicate an association with a lower predicted HRI. Point colours range from blue to red, representing low to high feature values. The vertical axis lists features ordered by mean absolute SHAP value, which highlights variables that contribute more strongly to model predictions overall.

The results indicate that VR, FAR, and NDVI have the largest mean absolute SHAP values and therefore constitute the most influential variables in explaining variation in predicted HRI. In terms of directionality, samples with higher FAR values are more frequently associated with positive SHAP values, which is consistent with higher development intensity being associated with higher predicted heat risk in the model. VR shows the opposite tendency, with higher VR values more often corresponding to negative SHAP

values and lower VR values to positive SHAP values, suggesting that higher vegetation ratio is generally associated with lower predicted HRI. By contrast, the SHAP distributions for NDVI and SR are more dispersed, indicating greater heterogeneity in their contributions across samples and implying that their predictive roles may be more context dependent, potentially varying with other urban morphological characteristics.

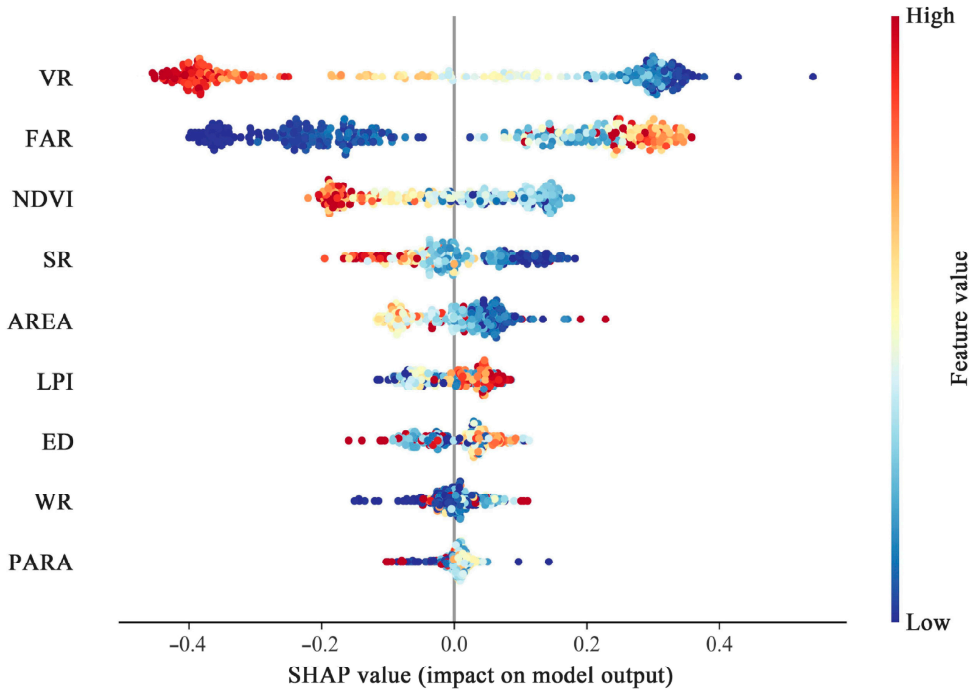

Figure 7. Feature importance of SHAP for urban morphological characteristics.

Building on the swarm plot, SHAP dependence plots were used to explore interaction patterns (Figure 8), with the FAR–SR and VR–SR pairings providing the most informative examples. In the FAR dependence plot, SHAP values generally shift from negative to positive as FAR increases from near zero to around 1.0, and then rise rapidly. As FAR increases further, SHAP values remain high but the rate of increase moderates, which is consistent with a diminishing marginal change in contribution within the model. When the points are coloured by SR, the FAR related pattern varies across SR levels. In the low FAR range, higher SR values tend to align with SHAP values closer to zero, whereas lower SR values more often coincide with clearly positive SHAP values. This suggests that the association between development intensity and predicted HRI may be stronger in contexts with lower SR levels, while it appears more muted when SR is higher. In the VR dependence plot, lower VR values are generally associated with positive SHAP values, whereas SHAP values decline as VR increases, indicating that higher vegetation ratio is associated with lower predicted HRI in the model. Colouring the scatter plot by SR shows limited stratification overall, with only modest differences in some VR intervals. This pattern suggests that SR may play a relatively minor moderating role in the VR-related relationship in this setting.

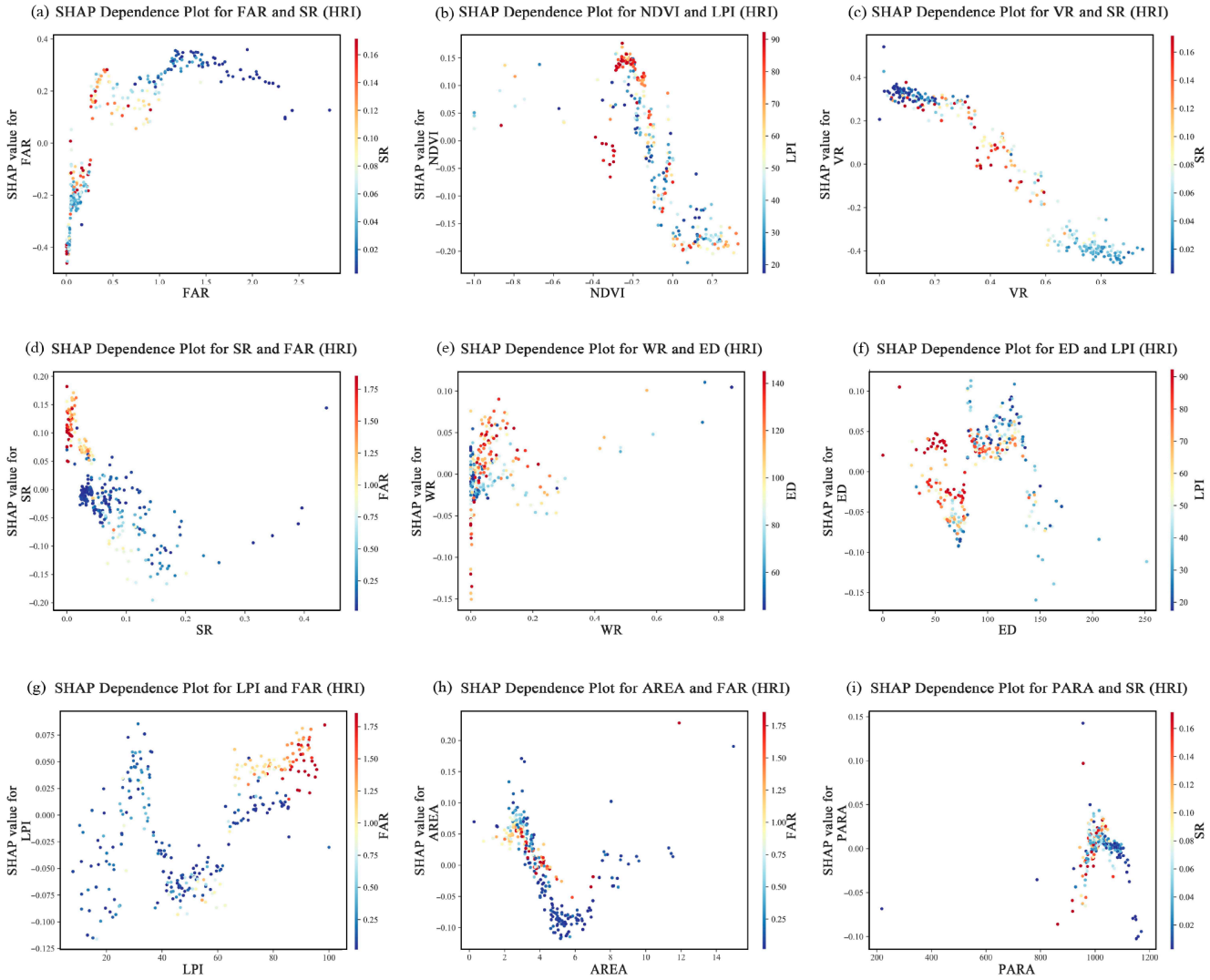

Figure 8. (**a**–**i**) SHAP scatter dependencies for urban morphological features.

5. Discussion

5.1. The Influence of Urban Morphological Characteristics on HRI

Traditional urban heat risk assessments often report that high-risk zones are concentrated in city centres. For example, a study in the United States found that peak heat risk index values were clustered in the Washington, D.C.-centred region [51]. Using a comprehensive disaster exposure vulnerability framework, Hua [52] similarly reported that high risk was concentrated in core urban areas during both daytime and night time, which differs to some extent from the pattern observed in this study. Although population density, road network density, and building age are often higher in central areas and may be associated with higher hazard, exposure, and vulnerability, city centres also tend to concentrate response resources, including public cooling facilities and better access to medical services. Central areas are also commonly characterised by higher levels of economic development and stronger public service provision. Together, these conditions are consistent with greater capacity to buffer and recover from heat related impacts, which may lower the overall heat risk classification under frameworks that explicitly account for adaptability. In addition, our results indicate that heat risk can be relatively higher in peripheral areas surrounding the urban core than in the core itself. These transitional zones may experience combined pressures related to built environment warming and population exposure, while having comparatively limited access to public services and health resources and weaker

community level resilience. Under such conditions, heat adaptability may be insufficient to offset other risk components, which offers spatially explicit guidance for targeting the allocation of cooling resources, healthcare services, and local emergency response capacity.

Moreover, existing evidence suggests that urban HRI exhibits pronounced spatial variability. A study of 139 cities in the Philippines reported that high HRI values tend to cluster in metropolitan regions. This pattern was attributed to the co-occurrence of elevated heat hazard and population exposure, together with uneven land cover and population distribution within these regions, leading to substantial differences in heat related health risk across cities and within individual urban areas [11]. Neighbourhood-scale studies further indicate that areas of high heat hazard do not necessarily coincide spatially with areas of high exposure or vulnerability. As a result, composite risk can emerge as multiple high-risk hotspots that are spatially misaligned across components [53]. In China, Zhou [54] similarly reported that heat hazards show clear intra-urban disparities and tend to be higher in more intensively developed areas. Our results are consistent with this pattern, and the geographically weighted machine learning analysis provides additional evidence that the strength of these associations can vary across space.

Although urban heat risk varies substantially across space, a growing body of evidence suggests that well-designed urban morphological planning and greening strategies are associated with meaningful heat risk reduction. A multi-city study covering 452 locations in 24 countries reported lower heat related mortality risk in greener cities, and estimated that a 20% increase in green space could reduce the proportion of heat related deaths attributable to heat stress by about 9% [55]. A large scale analysis of 11,534 urban areas similarly indicated that higher urban greenness is associated with lower average warm season temperatures, and scenario based assessments suggested a lower share of heat-related deaths under increased greening [56]. Beyond city-scale greenness, evidence also points to the importance of urban configuration. Using CFD simulations across multiple scenarios, Karimimoshaver et al. reported that a street canopy configuration with H/W = 1 and L/W = 2 was more effective for reducing temperatures and mitigating heat island intensity, providing quantitative reference values for street canopy design [57]. Wong et al. reported that ground-level greening is associated with reductions in peak surface temperature of about 2 to 9 °C, while green roofs and green walls can be associated with larger surface temperature reductions. They further emphasised that cooling benefits may be strengthened through configuration strategies such as more distributed park placement and increased tree coverage [58]. Health impact evidence at fine spatial resolution reinforces these implications. A high-resolution assessment across 93 European cities quantified the summer premature mortality burden associated with UHI and estimated the cooling potential and preventable deaths linked to increasing urban tree cover to 30% [59]. In addition, vegetation type and spatial scale appear to matter. Song [60] reported that forests are associated with stronger attenuation of heatwave related mortality risk than grasslands, with particularly notable effects around the 1 km scale of local exposure. Taken together, these studies suggest that integrated urban morphological planning, including both greening extent and spatial configuration, can contribute to reducing heat risk and supporting urban sustainability.

5.2. Urban Planning Implications

This study examined how heat risk is associated with multiple urban morphological characteristics and compared the relative importance of these characteristics within the modelling framework. The resulting evidence may inform ecosystem design and management, as well as urban planning, by clarifying which aspects of urban form are most closely linked to elevated heat risk.

In high-density built-up areas, planning and design interventions should give particular attention to heat stress associated with development intensity. Model results indicate that FAR is generally associated with higher predicted HRI across most streets. This pattern is consistent with the possibility that high intensity development is linked to more constrained ventilation, greater heat storage, and weaker nocturnal heat release. From an operational planning perspective, the implication is not simply to impose uniformly lower FAR. Instead, intensity management can be translated into more targeted spatial form guidance. In new development and renewal projects, it may be beneficial to avoid continuous and highly enclosed high density block interfaces. Heat transport and dissipation conditions may be improved by promoting massing variation, increasing block porosity and open space ratios, and optimising building spacing and street canyon geometry. In addition, high-risk areas can prioritise complementary measures such as roof and facade greening, shading systems, and higher albedo materials, which are commonly used to support cumulative cooling benefits.

Second, the planning relevance of green space allocation lies not only in increasing total area, but also in achieving effective levels of greening in priority locations. In this study, VR shows a relatively consistent association with predicted HRI and exhibits a clear inflection pattern in the dependence relationship. This suggests that vegetation ratio may need to exceed a minimum level before more stable heat risk reduction is reflected in the model. At the same time, the marginal contribution pattern of NDVI is more uncertain in some ranges, indicating that the cooling value of greenness may vary with background terrain and surrounding environmental context. Accordingly, greening strategies should prioritise high-risk and high-exposure streets rather than relying on uniform greening across the city. In peripheral urban areas and other identified hotspots, interventions can emphasise continuous tree canopy, street tree corridors, and community scale green networks. In ecologically dominated areas, maintaining the continuity and integrity of existing green space is important, because fragmentation may weaken local cooling functions that are already in place.

Third, the configuration of road networks and open spaces is associated with ventilation potential, which can be linked to differences in predicted heat risk. In this study, SR shows an overall negative association with predicted HRI, suggesting that streets with higher SR values tend to be characterised by lower modelled heat risk. This pattern is consistent with the possibility that denser and more connected street systems support air exchange and heat transport, thereby contributing to lower heat stress under certain urban contexts. In planning practice, both new development and regeneration projects should avoid large, enclosed superblocks and single-access layouts that may limit permeability and create unfavourable ventilation conditions. Where feasible, interventions can focus on improving minor road connectivity, opening selected cul-de-sacs, and strengthening continuous connections to open spaces so that ventilation corridors and pedestrian networks are more coherent. In areas where road network restructuring is constrained, microscale upgrades can be prioritised around ventilation related nodes, including squares, pocket parks, and waterfront open strips, to support local cooling at relatively low spatial cost.

Fourth, the contribution of blue spaces appears to be highly context-dependent, which highlights the importance of integration with the surrounding urban fabric rather than relying on isolated additions. In this study, water-related variables show higher predictive relevance only in certain locations, suggesting that water bodies are not uniformly associated with street-level heat risk across the city. From a planning perspective, it is therefore important to strengthen continuous networks that connect waterfront open strips with green space systems, street networks, and potential ventilation corridors. Such connectivity can reduce the likelihood that water bodies become functionally isolated within

high-density built environments, a condition that may limit their cooling influence. In parallel, accessibility and usability should be prioritised so that blue spaces can operate as practical heat exposure relief areas and risk buffering resources during heat events.

Finally, the geographically weighted model indicates that the dominant factors associated with HRI vary across streets. This suggests that planning interventions should adopt a zoned and differentiated approach rather than applying a uniform citywide strategy. On streets where development intensity is more strongly associated with higher heat risk, priority can be given to reducing heat accumulation through urban form constraints and renewal measures. On streets where vegetation conditions or ecological foundations play a larger predictive role, priority can be placed on protecting continuous green networks and improving shading capacity at key nodes through targeted greening. In waterfront areas or blue green resource clusters, interventions can focus on strengthening connectivity and enhancing the spillover of cooling benefits within integrated blue green networks. Embedding this logic of matching dominant factors with tailored strategies into regulatory planning controls, renewal guidelines, and assessments of public service and facility provision can help translate heat risk research into actionable spatial governance. This approach also supports more efficient allocation of limited resources by improving the marginal returns of targeted investments.

5.3. Limitations

This study has several limitations. First, heat hazard was primarily characterised using satellite-derived land surface temperature (LST). LST does not always correspond closely to near surface air temperature or to human experienced heat exposure, and discrepancies can arise under different land cover conditions and meteorological settings. Accordingly, heat risk interpretation based on LST should be treated with caution.

Second, the analysis focused on a single time window and a single-city case study, which limits its ability to represent interannual variability, the evolution of heatwave events, and temporal changes in heat adaptability, and also constrains the generalisability of the findings across urban contexts. In addition, the analysis was conducted at the street level; therefore, cross-scale sensitivity testing was not performed, and potential scale effects cannot be fully ruled out. Future work will prioritise extending the framework to multiple cities using harmonised datasets, and will incorporate multi-season and multi-year observations, as well as different times of day, to further examine the robustness of the findings.

Third, the HRI developed here is a composite index intended for spatial screening and relative comparison, rather than for the direct estimation of health outcomes. Accordingly, the index may be influenced by indicator selection, weighting choices, and data quality. Where feasible, external validation using independent health outcome datasets (e.g., heat-related mortality, hospital admissions, or emergency department visits) would strengthen the credibility of our interpretations; however, access to such individual-level records often requires appropriate ethical and legal approvals. In addition, future research should assess the transferability and temporal stability of the identified patterns and associations using multi-year and multi-city datasets.

Finally, although circularity is avoided by design, the morphology–HRI relationships identified by GW-XGBoost should be interpreted as associations rather than causal effects. Urban morphology may influence heat risk through multiple pathways, and unobserved factors (e.g., historical development trajectories, planning interventions, and socioeconomic processes) may jointly shape both morphology and risk, leading to potential confounding. Therefore, our findings are intended to provide interpretable, street-level associative evidence and spatial screening cues to support differentiated heat-risk governance and

hypothesis generation; causal identification would require longitudinal data or quasi-experimental designs.

6. Conclusions

This study examines the nonlinear associations between urban morphological characteristics and the heat risk index (HRI) at the street level in Tianjin under the HEVA framework. It characterises the patterns linked to key factors using marginal and interaction analyses, and it evaluates whether geographically weighted machine learning can help identify dominant variables and describe local variation in modelled relationships.

The results show that high HRI values in Tianjin are not confined to the most central areas. Instead, they are more prominent along the periphery of central districts and within transitional zones. This spatial pattern is consistent with the co-occurrence of relatively high heat hazard, exposure, and vulnerability, together with comparatively limited adaptive resource provision, which corresponds to higher composite risk.

Mechanism-oriented analyses indicate that development intensity, represented by FAR, is generally associated with higher HRI, whereas vegetation related indicators, including VR and NDVI, are generally associated with lower HRI. These associations are clearly nonlinear, and the marginal contribution patterns of key variables vary across value ranges. In addition, interaction patterns across different urban morphological contexts are associated with changes in the strength and extent of these relationships, which is consistent with spatial non-stationarity in street-level processes.

From a methodological perspective, GW-XGBoost improves error control while retaining interpretability and reveals spatial variation in dominant predictors at the street level. This provides an empirical basis for interpreting why conclusions may differ across studies conducted in different locations or with different spatial units. Overall, this study identifies heat risk hotspots, clarifies nonlinear associations between key urban morphological characteristics and heat risk, and characterises their marginal and interaction patterns. The findings provide evidence to support differentiated planning interventions, with particular attention to high-risk transitional zones.

Author Contributions: Conceptualization, Y.Z., J.W., K.Z. and S.Z.; methodology, Y.Z., J.W. and K.Z.; software, Y.Z. and J.W.; validation, Y.Z., J.W. and S.Z.; formal analysis, Y.Z. and J.W.; investigation, Y.Z., J.W. and Y.L.; resources, Y.Z., J.W. and Y.L.; data curation, Y.Z., J.W. and K.Z.; writing—original draft preparation, Y.Z., K.Z. and Q.W.; writing—review and editing, Y.Z., Y.Y. and Y.L.; visualization, Y.Z., Y.Y. and Q.W.; supervision, Y.Z., S.Z. and Y.L.; project administration, Y.Z. and Y.Y.; funding acquisition, Y.Z., K.Z. and Q.W. All authors have read and agreed to the published version of the manuscript.

Funding: This work was supported by the National Key Research and Development Program of China (2019YFD1100402).

Institutional Review Board Statement: Not applicable.

Informed Consent Statement: Not applicable.

Data Availability Statement: Data are contained within the article. The data presented in this study can be requested from the authors.

Conflicts of Interest: The authors declare no conflicts of interest.

Appendix A

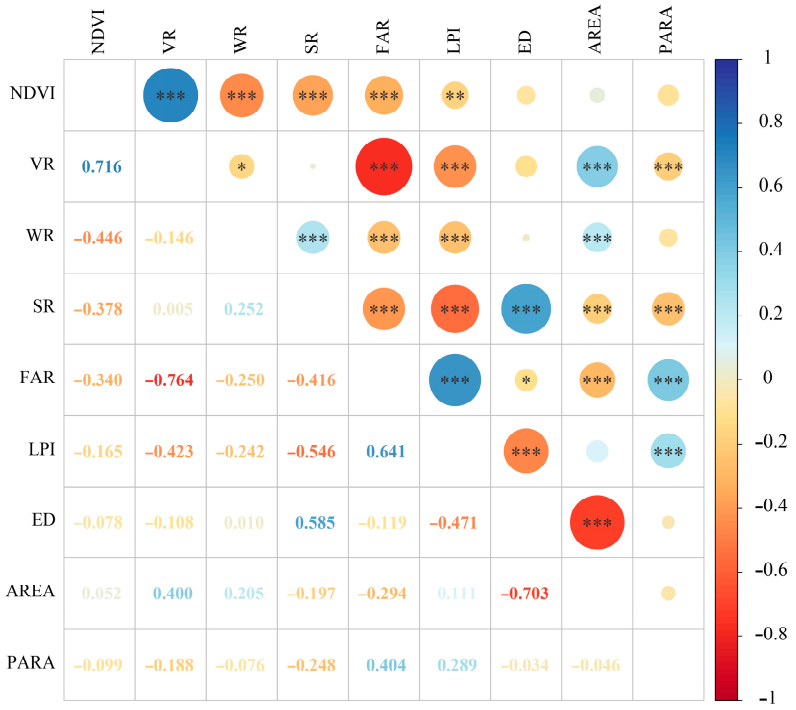

Figure A1. Pearson correlations among variables at the street level. Blue indicates positive correlations, whereas red indicates negative correlations. Larger squares represent stronger linear correlations between pairs of variables. Significance signs for correlation coefficients are marked in the circles: * denotes $p < 0.05$, ** denotes $p < 0.01$, *** denotes $p < 0.001$.

Appendix B

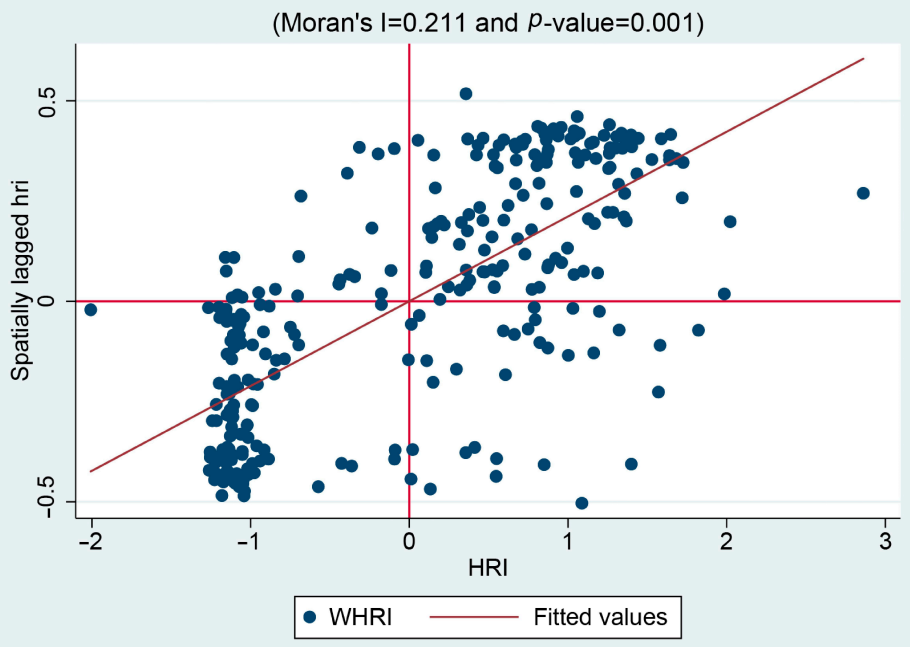

Figure A2. Moran scatterplot of HRI (Global Moran's I). The *x*-axis shows standardised HRI and the *y*-axis shows the spatial lag (Wz); the slope of the fitted line equals Global Moran's I. HRI exhibits significant positive spatial autocorrelation (Moran's I = 0.211, $p = 0.001$), indicating spatial clustering at the street level. The red diagonal line represents the linear fitted regression line in the Moran scatterplot.

References

1. Intergovernmental Panel on Climate Change. *Climate Change 2023: Synthesis Report*; Intergovernmental Panel on Climate Change: Geneva, Switzerland, 2023.
2. Perkins-Kirkpatrick, S.; Barriopedro, D.; Jha, R.; Wang, L.; Mondal, A.; Libonati, R.; Kornhuber, K. Extreme terrestrial heat in 2023. *Nat. Rev. Earth Environ.* **2024**, *5*, 244–246. [CrossRef]
3. Gasparrini, A.; Guo, Y.; Hashizume, M.; Lavigne, E.; Zanobetti, A.; Schwartz, J.; Tobias, A.; Tong, S.; Rocklöv, J.; Forsberg, B.; et al. Mortality risk attributable to high and low ambient temperature: A multicountry observational study. *Lancet* **2015**, *386*, 369–375. [CrossRef]
4. Vicedo-Cabrera, A.M.; Scovronick, N.; Sera, F.; Royé, D.; Schneider, R.; Tobias, A.; Astrom, C.; Guo, Y.; Honda, Y.; Hondula, D.M.; et al. The burden of heat-related mortality attributable to recent human-induced climate change. *Nat. Clim. Change* **2021**, *11*, 492–500. [CrossRef]
5. Wang, Y.; Wang, A.; Zhai, J.; Tao, H.; Jiang, T.; Su, B.; Yang, J.; Wang, G.; Liu, Q.; Gao, C.; et al. Tens of thousands additional deaths annually in cities of China between 1.5 °C and 2.0 °C warming. *Nat. Commun.* **2019**, *10*, 3376. [CrossRef]
6. World Health Organization. *Heat-Health Action Plans: Guidance*; World Health Organization Regional Office for Europe: Geneva, Switzerland, 2008.
7. Mondal, N.; Anand, P. Influence of Urbanization on Heat Exposure Risk across Indian Cities. *Sustain. Cities Soc.* **2025**, *135*, 106960. [CrossRef]
8. Oke, T.R. The energetic basis of the urban heat island. *Q. J. R. Meteorolog. Soc.* **1982**, *108*, 1–24. [CrossRef]
9. Stewart, I.; Oke, T. Local Climate Zones for Urban Temperature Studies. *Bull. Am. Meteorol. Soc.* **2012**, *93*, 1879–1900. [CrossRef]
10. Hsu, A.; Sheriff, G.; Chakraborty, T.; Manya, D. Disproportionate exposure to urban heat island intensity across major US cities. *Nat. Commun.* **2021**, *12*, 2721. [CrossRef]
11. Estoque, R.C.; Ooba, M.; Seposo, X.T.; Togawa, T.; Hijioka, Y.; Takahashi, K.; Nakamura, S. Heat health risk assessment in Philippine cities using remotely sensed data and social-ecological indicators. *Nat. Commun.* **2020**, *11*, 1581. [CrossRef]
12. Crichton, D. The risk triangle. In *Natural Disaster Management*; Tudor Rose: London, UK, 1999.
13. Ma, L.; Huang, G.; Johnson, B.A.; Chen, Z.; Li, M.; Yan, Z.; Zhan, W.; Lu, H.; He, W.; Lian, D. Investigating urban heat-related health risks based on local climate zones: A case study of Changzhou in China. *Sustain. Cities Soc.* **2023**, *91*, 104402. [CrossRef]
14. Xiang, Y.; Yuan, C.; Cen, Q.; Huang, C.; Wu, C.; Teng, M.; Zhou, Z. Heat risk assessment and response to green infrastructure based on local climate zones. *Build. Environ.* **2024**, *248*, 111040. [CrossRef]
15. Guo, R.; Guo, F.; Dong, J.; Wang, Z.; Zheng, R.; Zhang, H. Finer-scale urban health risk assessment based on the interaction perspective of thermal radiation, human, activity, and space. *Front. Archit. Res.* **2024**, *13*, 682–697. [CrossRef]
16. Chen, J.; Shi, X.; Shi, Y.; Delina, L.L. Assessing heat vulnerability risk of Jinan and Guangzhou's older populations based on multisource remote sensing data. *Build. Environ.* **2025**, *271*, 112622. [CrossRef]
17. Wu, H.; Xu, Y.; Zhang, M.; Su, L.; Wang, Y.; Zhu, S. Spatially explicit assessment of the heat-related health risk in the Yangtze River Delta, China, using multisource remote sensing and socioeconomic data. *Sustain. Cities Soc.* **2024**, *104*, 105300. [CrossRef]
18. Li, F.; Yigitcanlar, T.; Nepal, M.; Thanh, K.N.; Dur, F. Understanding Urban Heat Vulnerability Assessment Methods: A PRISMA Review. *Energies* **2022**, *15*, 6998. [CrossRef]
19. Gong, F.-Y.; Yang, Z.; Deng, S. Fine-scale assessment of diurnal heat health risk based on satellite and street view images. *Cities* **2025**, *162*, 105963. [CrossRef]
20. Xin, J.; Yang, J.; Jiang, Y.; Shi, Z.; Jin, C.; Xiao, X.; Xia, J.C.; Yang, R. Variations of Urban Thermal Risk with Local Climate Zones. *Int. J. Environ. Res. Public Health* **2023**, *20*, 3283. [CrossRef]
21. Liu, X.; Yue, W.; Yang, X.; Hu, K.; Zhang, W.; Huang, M. Mapping Urban Heat Vulnerability of Extreme Heat in Hangzhou via Comparing Two Approaches. *Complexity* **2020**, *2020*, 9717658. [CrossRef]
22. Zhou, B.; Rybski, D.; Kropp, J.P. The role of city size and urban form in the surface urban heat island. *Sci. Rep.* **2017**, *7*, 4791. [CrossRef]
23. Chen, Z.; Ye, J.; Liu, Y.; Hu, T.; Dong, J. Global assessment in the effect of urban built-up environment on cooling efficiency of green spaces. *Commun. Earth Environ.* **2025**, *6*, 968. [CrossRef]
24. Huang, X.; Wang, Y. Investigating the effects of 3D urban morphology on the surface urban heat island effect in urban functional zones by using high-resolution remote sensing data: A case study of Wuhan, Central China. *ISPRS J. Photogramm. Remote Sens.* **2019**, *152*, 119–131. [CrossRef]
25. Yang, L.; Yu, K.; Ai, J.; Liu, Y.; Yang, W.; Liu, J. Dominant Factors and Spatial Heterogeneity of Land Surface Temperatures in Urban Areas: A Case Study in Fuzhou, China. *Remote Sens.* **2022**, *14*, 1266.
26. Liu, Y.; Chen, H.; Wu, J.; Wang, Y.; Ni, Z.; Chen, S. Impact of urban spatial dynamics and blue-green infrastructure on urban heat islands: A case study of Guangzhou using Local Climate Zones and predictive modeling. *Sustain. Cities Soc.* **2024**, *115*, 105819. [CrossRef]

27. Werner, M.; Dax, G.; Laass, M. Computational challenges for artificial intelligence and machine learning in environmental research. In *Proceedings of the INFORMATIK 2020*; Gesellschaft für Informatik: Bonn, Germany, 2021.
28. Ye, M.; Zhu, L.; Li, X.; Ke, Y.; Huang, Y.; Chen, B.; Yu, H.; Li, H.; Feng, H. Estimation of the soil arsenic concentration using a geographically weighted XGBoost model based on hyperspectral data. *Sci. Total Environ.* **2023**, *858*, 159798. [CrossRef]
29. Georganos, S.; Grippa, T.; Niang Gadiaga, A.; Linard, C.; Lennert, M.; Vanhuysse, S.; Mboga, N.; Wolff, E.; Kalogirou, S. Geographical random forests: A spatial extension of the random forest algorithm to address spatial heterogeneity in remote sensing and population modelling. *Geocarto Int.* **2021**, *36*, 121–136. [CrossRef]
30. Grekousis, G.; Feng, Z.; Marakakis, I.; Lu, Y.; Wang, R. Ranking the importance of demographic, socioeconomic, and underlying health factors on US COVID-19 deaths: A geographical random forest approach. *Health Place* **2022**, *74*, 102744. [CrossRef]
31. Grekousis, G. Geographical-XGBoost: A new ensemble model for spatially local regression based on gradient-boosted trees. *J. Geogr. Syst.* **2025**, *27*, 169–195. [CrossRef]
32. Cresswell, K. A Florida urban heat risk index: Assessing weighting and aggregation approaches. *Urban Clim.* **2023**, *51*, 101646. [CrossRef]
33. Tianjin Municipal Bureau of Statistics. *Tianjin Statistical Yearbook 2023*; China Statistics Press: Beijing, China, 2023.
34. Ministry of Civil Affairs of the People's Republic of China. Administrative Division Codes of the People's Republic of China. Available online: http://www.mca.gov.cn (accessed on 8 February 2026).
35. Compiled by National Bureau of Statistics of China. *China Statistical Yearbook 2024*; China Statistics Press: Beijing, China, 2024.
36. Che, Y.; Li, X.; Liu, X.; Wang, Y.; Liao, W.; Zheng, X.; Zhang, X.; Xu, X.; Shi, Q.; Zhu, J.; et al. 3D-GloBFP: The first global three-dimensional building footprint dataset. *Earth Syst. Sci. Data* **2024**, *16*, 5357–5374. [CrossRef]
37. Zhang, Y.; Zhao, H.; Long, Y. CMAB: A Multi-Attribute Building Dataset of China. *Sci. Data* **2025**, *12*, 430. [CrossRef]
38. Xu, X. *China GDP Spatial Distribution Kilometer-Grid Dataset [Data Set]*; Resource and Environment Science Data Registration and Publishing System: Beijing, China, 2017.
39. Dow, K.; Cutter, S.L. Crying wolf: Repeat responses to hurricane evacuation orders. *Coast. Manag.* **1998**, *26*, 237–252. [CrossRef]
40. Koks, E.E.; Jongman, B.; Husby, T.G.; Botzen, W.J.W. Combining hazard, exposure and social vulnerability to provide lessons for flood risk management. *Environ. Sci. Policy* **2015**, *47*, 42–52. [CrossRef]
41. Wang, S.; Sun, Q.C.; Huang, X.; Tao, Y.; Dong, C.; Das, S.; Liu, Y. Health-integrated heat risk assessment in Australian cities. *Environ. Impact Assess. Rev.* **2023**, *102*, 107176. [CrossRef]
42. Li, C.; Yu, Z.; Yuan, Y.; Geng, X.; Zhang, D.; Zheng, X.; Li, R.; Sun, W.; Wang, X. A synthetic water-heat-vegetation biodiversity nexus approach to assess coastal vulnerability in eastern China. *Sci. Total Environ.* **2022**, *845*, 157074. [CrossRef]
43. Zhang, R.; Yang, J.; Ma, X.; Xiao, X.; Xia, J. Optimal allocation of local climate zones based on heat vulnerability perspective. *Sustain. Cities Soc.* **2023**, *99*, 104981. [CrossRef]
44. Zhang, W.; Zheng, C.; Chen, F. Mapping heat-related health risks of elderly citizens in mountainous area: A case study of Chongqing, China. *Sci. Total Environ.* **2019**, *663*, 852–866. [CrossRef]
45. Thorsson, S.; Rocklöv, J.; Konarska, J.; Lindberg, F.; Holmer, B.; Dousset, B.; Rayner, D. Mean radiant temperature—A predictor of heat related mortality. *Urban Clim.* **2014**, *10*, 332–345. [CrossRef]
46. Zhu, Q.; Liu, T.; Lin, H.; Xiao, J.; Luo, Y.; Zeng, W.; Zeng, S.; Wei, Y.; Chu, C.; Baum, S.; et al. The spatial distribution of health vulnerability to heat waves in Guangdong Province, China. *Glob. Health Action* **2014**, *7*, 25051. [CrossRef]
47. Cai, Z.; Tang, Y.; Chen, K.; Han, G. Assessing the Heat Vulnerability of Different Local Climate Zones in the Old Areas of a Chinese Megacity. *Sustainability* **2019**, *11*, 2032. [CrossRef]
48. Fan, J.; Wang, X.; Wu, L.; Zhou, H.; Zhang, F.; Yu, X.; Lu, X.; Xiang, Y. Comparison of Support Vector Machine and Extreme Gradient Boosting for predicting daily global solar radiation using temperature and precipitation in humid subtropical climates: A case study in China. *Energy Convers. Manag.* **2018**, *164*, 102–111. [CrossRef]
49. Xia, Y.; Liu, C.; Li, Y.; Liu, N. A boosted decision tree approach using Bayesian hyper-parameter optimization for credit scoring. *Expert Syst. Appl.* **2017**, *78*, 225–241. [CrossRef]
50. Fisher, A.; Rudin, C.; Dominici, F. All Models are Wrong, but Many are Useful: Learning a Variable's Importance by Studying an Entire Class of Prediction Models Simultaneously. *J. Mach. Learn. Res.* **2019**, *20*, 1–81.
51. Aubrecht, C.; Özceylan, D. Identification of heat risk patterns in the U.S. National Capital Region by integrating heat stress and related vulnerability. *Environ. Int.* **2013**, *56*, 65–77. [CrossRef] [PubMed]
52. Hua, J.; Zhang, X.; Ren, C.; Shi, Y.; Lee, T.-C. Spatiotemporal assessment of extreme heat risk for high-density cities: A case study of Hong Kong from 2006 to 2016. *Sustain. Cities Soc.* **2021**, *64*, 102507. [CrossRef]
53. Yu, W.; Zhu, J.; Zhou, W.; Wang, W. Spatial heterogeneity of the integrated risks of urban heat stress and flooding strike. *Sci. Total Environ.* **2024**, *954*, 176517. [CrossRef]
54. Zhou, Y.; Zhang, G.; Jiang, L.; Chen, X.; Xie, T.; Wei, Y.; Xu, L.; Pan, Z.; An, P.; Lun, F. Mapping local climate zones and their associated heat risk issues in Beijing: Based on open data. *Sustain. Cities Soc.* **2021**, *74*, 103174. [CrossRef]

55. Choi, H.M.; Lee, W.; Roye, D.; Heo, S.; Urban, A.; Entezari, A.; Vicedo-Cabrera, A.M.; Zanobetti, A.; Gasparrini, A.; Analitis, A.; et al. Effect modification of greenness on the association between heat and mortality: A multi-city multi-country study. *EBioMedicine* **2022**, *84*, 104251. [CrossRef]
56. Wu, Y.; Wen, B.; Ye, T.; Huang, W.; Liu, Y.; Gasparrini, A.; Sera, F.; Tong, S.; Lavigne, E.; Roye, D.; et al. Estimating the urban heat-related mortality burden due to greenness: A global modelling study. *Lancet Planet. Health* **2025**, *9*, 101235. [CrossRef]
57. Karimimoshaver, M.; Khalvandi, R.; Khalvandi, M. The effect of urban morphology on heat accumulation in urban street canyons and mitigation approach. *Sustain. Cities Soc.* **2021**, *73*, 103127. [CrossRef]
58. Wong, N.H.; Tan, C.L.; Kolokotsa, D.D.; Takebayashi, H. Greenery as a mitigation and adaptation strategy to urban heat. *Nat. Rev. Earth Environ.* **2021**, *2*, 166–181. [CrossRef]
59. Iungman, T.; Cirach, M.; Marando, F.; Pereira Barboza, E.; Khomenko, S.; Masselot, P.; Quijal-Zamorano, M.; Mueller, N.; Gasparrini, A.; Urquiza, J.; et al. Cooling cities through urban green infrastructure: A health impact assessment of European cities. *Lancet* **2023**, *401*, 577–589. [CrossRef] [PubMed]
60. Song, J.; Gasparrini, A.; Wei, D.; Lu, Y.; Hu, K.; Fischer, T.B.; Nieuwenhuijsen, M. Do greenspaces really reduce heat health impacts? Evidence for different vegetation types and distance-based greenspace exposure. *Environ. Int.* **2024**, *191*, 108950. [CrossRef] [PubMed]

Disclaimer/Publisher's Note: The statements, opinions and data contained in all publications are solely those of the individual author(s) and contributor(s) and not of MDPI and/or the editor(s). MDPI and/or the editor(s) disclaim responsibility for any injury to people or property resulting from any ideas, methods, instructions or products referred to in the content.